






## Volumetric visualization of vanishing vortices in wind turbine wakes

Johannes N. Hillestad <sup>\*</sup>, Srikar Yadala , Ingrid Neunaber , Leon Li,  
R. Jason Hearst <sup>†</sup> and Nicholas A. Worth <sup>‡</sup>  
*Department of Energy and Process Engineering,  
Norwegian University of Science and Technology, N-7491 Norway*



(Received 19 October 2023; accepted 25 March 2024; published 31 May 2024)

Volumetric velocimetry is used to investigate the evolution of tip vortices in the wake of a model wind turbine. The power spectral density of streamwise velocity fluctuations is estimated at several downstream locations, and changes in the magnitude of the frequency peaks corresponding to the blade-pass and turbine rotational frequency are observed. Full volumetric visualization of the coherent structures depicts the vortex merging process responsible for the change in detected frequency peaks, capturing the physical mechanism likely responsible for many similar previous observations.

DOI: [10.1103/PhysRevFluids.9.L052701](https://doi.org/10.1103/PhysRevFluids.9.L052701)

Fluid flow around a rotor blade generates lift, which is linked to bound circulation around the blade. A radial gradient of this bound circulation along the rotor blade's span leads some of the associated vorticity to be shed into the wake downstream, particularly at the tip. This is the origin of tip vortices in wind turbine (WT) wakes. One tip vortex is shed from each of the  $N$  blades of a WT, which are advected downstream by the mean flow, forming a helical vortex system. For identical rotor blades and uniform inflow conditions, the tip vortices are similar. Thus, for a WT rotating at a rotor frequency  $f_R$ , one would expect to observe a dominant spectral signature at  $N \cdot f_R$ , or the so-called blade-pass frequency  $f_{BP}$  in the WT's wake. However, such a signature is completely absent in numerous field and laboratory studies (see [1–3]). Given the importance of tip-vortex dynamics in downstream wake recovery, and ultimately, wind-farm design, such a feature cannot be overlooked. Therefore, the objective of the present investigation is to elucidate the physical origin of this enigma, so that there will be no more tilting at windmills [4], at least concerning tip vortices.

The evolution, interaction, and breakdown of tip vortices have been studied extensively for both wind turbines [5,6] and propellers [7]. Tip vortices of equal strength begin interacting as they move downstream and reciprocally influence each other based on mutual inductance, as observed experimentally [6], and consistently in numerical simulations [8–13]. Several experimental studies that investigate the general evolution of wind turbine wakes contain results (often in the form of spectra computed from point measurements such as hot-wire anemometry or flow visualization) through which conclusions are drawn regarding the behavior of tip vortices. These studies cover

---

\*johannes.n.hillestad@ntnu.no

†jason.hearst@ntnu.no

‡nicholas.a.worth@ntnu.no

a range of conditions including various rotor configurations (two or three bladed), inflow velocity profiles (uniform or boundary layer), inflow turbulence intensities, rotor diameters, and Reynolds numbers. Unlike simulations, the experimental findings do not all converge and can be broadly classified into three categories. In category (1), as expected, dominant spectral peaks are detected at  $f_{BP}$  and, sometimes, its harmonics [14,15]. Some studies [7,16–19] demonstrate identical vortices interacting, therefore falling (presumably) into the same category. In category (2), spectral content at both  $f_{BP}$  and  $f_R$  are found [20–25]. Finally, in category (3), the dominant peak is at  $f_R$  [1–3]. Here, the results sometimes also show harmonics of  $f_R$ , but not a peak at  $f_{BP}$ . Interestingly, Toloui *et al.* [1] conducted a field study on a utility-scale turbine where similar observations were made. Thus, this puzzling phenomenon of missing spectral signature at  $f_{BP}$  does not only apply to laboratory-scale WTs, but can also feature in utility-scale turbines. Upstream of the tip-vortex merging, detection of any spectral peak other than  $f_{BP}$  is worth looking further into as theoretically, in this region of the flow, no spectral peak at  $f_R$  should be detected at all.

The complexity of WT wake flow dynamics is well known, but previous literature exhibits some ambivalence with respect to explaining a dominant spectral peak at  $f_R$  (categories 2 and 3). Such observations are not always discussed, and if they are, a variety of explanations are commonly given. First, a stronger peak at  $f_R$  and dampening of  $f_{BP}$  have been observed with increasing Reynolds number [1,20]. Second, the spectral signature of tip vortices depends on the WT wake measurement location and its tip-speed ratio. As these vortical structures interact and merge downstream, a shift from a spectral peak at  $f_{BP}$  toward  $f_R$  is expected [1,7]. Finally, varying vortex strength and vortex wandering have also been named as causes for a dominant peak at  $f_R$  [2,26]. Mechanical reasons such as differences in the blade angle of attack (AoA) or manufacturing tolerances are often given as justifications for this. Here, the focus will be on the effect of difference in blade AoA.

This Letter presents an experimental investigation of the near wake behind a model WT, to understand the physical mechanisms underlying the disappearing spectral peak at  $f_{BP}$ . In an effort to better reproduce conditions present in real WT flows, freestream turbulence was introduced. Time-resolved volumetric velocity data was acquired to circumvent the point-measurement issue, which enables us to probe the spectral content at any wake location, simultaneously. Unlike more common planar experimental measurements, volumetric measurements also allow the vortical structures behind each blade to be captured, enabling us to decouple their formation, evolution, and interaction. By setting different AoAs for each blade of the turbine, the observed shift/absence of spectral peaks is provoked. This Letter demonstrates how differences in the blade AoA can alter tip vortex formation and interaction, elucidating the origin of the missing spectral peak.

The experiments were conducted in the water channel facility at the Norwegian University of Science and Technology which houses an active grid with a mesh length of  $M = 100$  mm at the beginning of the test section [27,28]. By leveraging the principle of dynamic similarity, this experiment was undertaken in water. The use of water permits better implementation of the volumetric velocimetry technique described later in this section.

A freely rotating, two-bladed model WT with rotor diameter  $D = 45$  mm, which was used and characterized well in previous research efforts [29–33], was used in the current experiment. The rotor blades are thin, cambered plates with a maximum chord length of 8 mm and a maximum thickness of 0.5 mm. At the operating Reynolds number, the WT has a drag coefficient of  $C_D \approx 0.5$ . Further details of this model WT can be found in the aforementioned studies [29–33]. The tolerances between the nacelle shaft and the rotor’s center mounting hole allowed the rotor’s rotation axis and the nacelle direction vector to not be colinear. This feature was utilized to obtain the difference in blade AoA. The turbine was mounted inverted on the underside of an acrylic mounting plate with dimensions 3000 mm  $\times$  1800 mm  $\times$  10 mm. This plate was positioned 480 mm from the channel floor, with the leading edge  $28.9M$  downstream of the active grid. A sharp leading edge minimizes the recirculation zone at the front of the plate, after which the developing boundary layer was tripped. The WT was positioned  $8.5M$  downstream of the plate’s leading edge and  $37.4M$  downstream of the active grid, in the center of the channel’s span. This streamwise location was chosen as the freestream turbulence was approximately homogenous and isotropic [27]. A WT hub

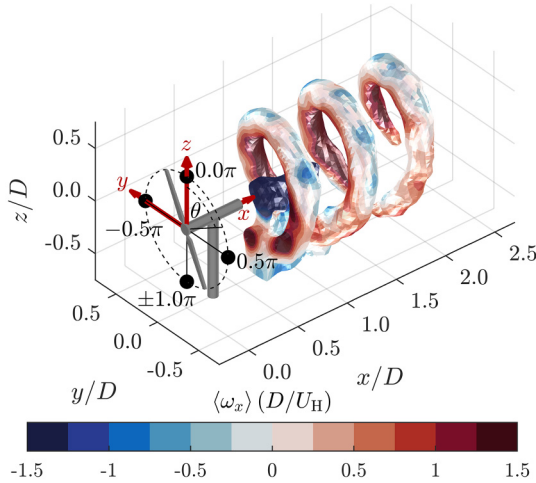


FIG. 1. Coordinate systems and an isosurface of  $\langle \omega \rangle$  is shown. The isosurface is colored by  $\langle \omega_x \rangle$ . For visual clarity, the isosurface has been masked for  $x/D < 0.7$ .

height of  $H_H = 160$  mm ensured that the rotor was in the homogeneous freestream and outside the boundary layers developing along the channel floor and the underside of the mounting plate. The water head was maintained at  $H_w = 0.5$  m during the experiment, which ensured that the entire setup was completely submerged. Freestream reference quantities were measured using a laser Doppler velocimetry probe positioned  $5D$  upstream of the WT. The freestream velocity was maintained at  $U_H = 0.4$  m/s. The resulting Reynolds number based on the rotor diameter is  $Re_D \approx 2 \times 10^4$ . While this Reynolds number is lower than that of a full-scale WT, it has been shown that the physical phenomena which occur in the outer shell of the near wake of a WT are captured well in scale experiments [34]. As this study only considers phenomena which occur in the outer shell of the wake, the conclusions should be applicable to full-scale WTs as well. The active grid was used to elevate the freestream turbulence intensity to 5% to demonstrate robustness of the observed phenomenon to incoming disturbances experienced by utility-scale WTs, where the turbulence intensity was chosen based on turbulence intensities present in real WT flows [35]. The resulting integral length scale is 60 mm, which is on the order of the turbine diameter ( $60 \text{ mm} \approx 1.3D$ ). While any further variation in turbulence levels and/or introduction of shear layers would likely influence the results, this was considered to be outside the scope of this study and will therefore not be discussed further here.

The Cartesian coordinate system  $(x, y, z)$  employed here is shown in Fig. 1. The velocities in the  $x$ ,  $y$ , and  $z$  directions are  $u$ ,  $v$ , and  $w$ , respectively. A cylindrical coordinate system  $(x, r, \theta)$ , also shown in Fig. 1, will also be used whenever advantageous.

Quantitative three-dimensional velocity data was obtained through time-resolved particle tracking velocimetry based on the shake-the-box (STB) algorithm [36]. The volume-of-interest (VOI) was illuminated by eight GS Vitec MultiLED QT LED heads ( $8 \times 150$  W). Polystyrene spheres with a mean diameter of  $40 \mu\text{m}$  and a density of  $\rho \approx 1000 \text{ kg/m}^3$  served as neutrally buoyant tracer particles. Particle images were obtained using four Photron FASTCAM Mini WX100 ( $2048 \times 2048$  pixels) cameras. These were equipped with Sigma 180 mm F/3.5 EX APO Macro DG HSM lenses operated at  $f_\# = 16$  to obtain the required depth of field. The cameras were arranged in a linear configuration with a  $20^\circ$  angular separation, viewing the VOI through optical prisms to correct for light refraction. The LEDs and cameras were synchronized with a LaVision PTU X controller. The cameras were operated at a sampling rate of  $f_s = 500$  Hz for a total of 5457 exposures.

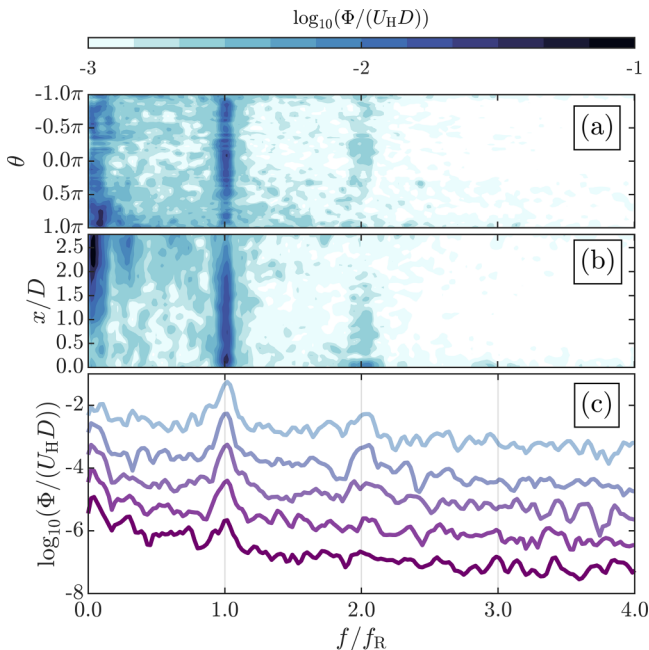


FIG. 2. Nondimensionalized PSD,  $\Phi$ , in the WT's wake. (a) Spectrogram at  $x/D = 1$ , at radial position  $r/D = 0.45$ ; (b) Spectrogram at  $r/D = 0.45$  and  $\theta = 0.0\pi$ , along the  $x/D$ ; (c) PSD line plots at  $r/D = 0.45$  and  $x/D = 0.5, 1.0, 1.5, 2.0,$  and  $2.5$  from top to bottom. For visual clarity, the line plots in panel (c) have been separated by one order of magnitude. The topmost line at  $x/D = 0.5$  is not shifted.

Data acquisition, calibration, and processing were performed using DaVis 10.1. The initial calibration was obtained using a two-level calibration plate (LaVision Typ 20) and a third-order polynomial model. Volume self-calibration [37] was applied iteratively on a subset of the acquired particle images until the calibration error was below 0.1 pixels. The optical transfer function [38] was then calculated on the same subset. Following this, Lagrangian particle tracks were calculated using the STB algorithm. The error in  $u$ ,  $v$ , and  $w$  from the STB algorithm is 2% of the freestream velocity [39]. From these, Eulerian velocity fields were obtained using the VIC# technique [40]. The resultant VOI was  $135 \text{ mm} \times 100 \text{ mm} \times 125 \text{ mm}$  ( $3.0D \times 2.2D \times 2.8D$ ) along the  $x$ ,  $y$ , and  $z$  directions, respectively, with a vector spacing of 1.6 mm in all three directions.

The rotor frequency  $f_R$  was measured through motion tracking of the turbine blades in the acquired time series and is  $f_R = 11.3 \text{ Hz}$ . The blade-pass frequency is expected to be  $f_{BP} = 2f_R = 22.6 \text{ Hz}$ . The tip speed ratio is  $\lambda = \frac{2\pi f_R D/2}{U_H} \approx 4$ . The time series of angular blade positions (along  $\theta$ ) from this motion tracking was also used to perform temporal binning of the velocity vector fields to compute phase-averaged fields, represented henceforth by  $\langle \cdot \rangle$ , along one full rotation of the rotor. An isosurface of the vorticity magnitude computed at one of the phases is presented in Fig. 1. Common features of a WT wake such as the hub and tip vortices are evident.

The same motion tracking images were used to determine the AoA of the blade tips. Based on visual inspection and WT momentum theory, the AoAs of the blades were  $0$  and  $10^\circ$ , respectively. These AoAs stayed consistent throughout the measurement period.

The nondimensionalized power spectral density (PSD),  $\Phi$ , computed from the streamwise velocity fluctuations at various locations, is presented in Fig. 2. The final frequency resolution was  $\Delta f = 0.25 \text{ Hz}$ , and all frequencies are hereafter nondimensionalized with  $f_R$ . Spectra of other velocity components and vorticity components were also calculated. As they show the same trends, only the spectra calculated from the streamwise velocity are presented and discussed.

The spectrogram computed at  $x/D = 1$  along the radial position  $r/D = 0.45$  is presented in Fig. 2(a). Fluctuations with the highest energy are observed at  $f_R$  at all azimuthal positions  $\theta$ . Spectral content is also observed around  $f/f_R = 2$ , which corresponds to  $f_{BP}$  of the two-bladed model WT used here. However, it is noteworthy that the energy of fluctuations around  $f_{BP}$  are approximately two orders-of-magnitude lower when compared to  $f_R$ .

The evolution of these fluctuations along the streamwise direction is studied through the spectrogram in Fig. 2(b) computed at  $r/D = 0.45$  and  $\theta = 0.0\pi$ . Example spectra at five different streamwise stations are presented in Fig. 2(c). Fluctuations at  $f_R$  are observed in the entire measured domain and are seen to contain the highest energy. The most interesting features pertain to  $f_{BP}$ . While always being weaker than  $f_R$ , they seem to decrease in strength from  $x/D = 0$  to  $x/D \approx 1.5$ , after which they vanish completely, similar to findings in [1–3].

The spectral peak at  $f_{BP}$  indicates that two tip vortices are present close to the WT. The relative weakness of this peak in comparison with that at  $f_R$  is a consequence of the difference in blade AoA. While the decrease in the peak at  $f_{BP}$  with downstream location is natural [25,26], it disappearing completely for  $x/D > 1.5$  is unconventional. Nonetheless, the spectra reveal that the current findings are similar to those from category (2) [20–25] until  $x/D \approx 1.5$  and resemble studies in category (3) [1–3] farther downstream. This exercise demonstrates that given the complex nature of the flow in a WT's wake, the measurement location can potentially obscure information regarding the true nature of the ensuing dynamics. This issue can be compounded when measurements are acquired at only a few locations in the WT's wake.

The cause of these observations in the spectral analysis can be elucidated by studying the velocity fields themselves, specifically the behavior and dynamics of vortical structures in the model WT's wake using the time-resolved volumetric data acquired here. To this end, the vortical structures in the phase-average fields are investigated further. The nonlinearities and complex features of a WT wake flow originate from the advective acceleration term in the Navier-Stokes equation. This term can be written as the sum of the Lamb vector,  $\mathbf{L} = \boldsymbol{\omega} \times \mathbf{u}$  [41], and the gradient of kinetic energy. The latter only contains acceleration terms that lead to pure compression/expansion. All the shear acceleration terms, the terms that lead to rotation and shear, originate from the Lamb-vector term [41]. As a WT wake is a region of organized vortical flow with high levels of shear and rotation, the Lamb vector magnitude is chosen as the vortex-identification criterion. This parameter is also chosen because the detected structures appear more compact and localized in space [42], which is necessary to study a complex flow field, such as a WT wake.

Isosurfaces of the phase-averaged Lamb vector magnitude  $\langle |\mathbf{L}| \rangle (D/U_H^2) = 0.7$  are presented in Fig. 3. Figure 3(a) shows the entire measurement domain. Two tip vortices (cyan and green isosurfaces), one shed from each turbine blade, are clearly observed for  $x/D \lesssim 1$ . However, the green tip vortex appears to be smaller than the cyan one. The cyan and green tip vortices are shed by the blades with blades at  $0$  and  $10^\circ$  AoA, respectively. The discrepancy occurs during vortex formation and can be attributed to the difference in AoA. At the tips, the rotor blade is a thin, cambered plate. Based on aerodynamic characteristics for thin plates with small camber, the blade producing the cyan structure is generating lift, while the other is stalled [43,44]. This results in tip vortices of different strengths and sizes, and is expected to be the reason for lower spectral energy in the  $f_{BP}$  frequency band compared to  $f_R$  in Fig. 2, until  $x/D = 1.5$ , although in this region a peak is observed at both.

As the flow advects the tip vortices downstream, the position of the green tip vortex relative to the cyan vortex changes. This is apparent from the four snapshots around the top-tip position presented in Figs. 3(b)–3(e). The panels show how the green tip vortex moves from being close to the upstream cyan vortex to being closer to the downstream cyan vortex. This indicates that the green tip vortex is advected at a higher velocity. Differences in downstream advection velocity between adjacent vortices can occur during leapfrogging [6], in which adjacent vortices switch order due to mutual induction. This process can be affected when the vortex characteristics differ, for example due to dynamic induction control [19]. In the present study, the different advection velocities are likely to

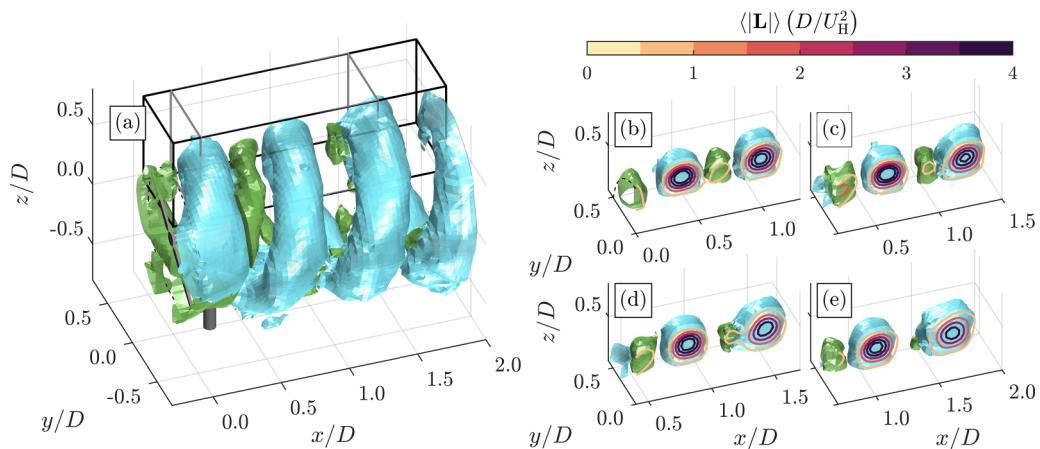


FIG. 3. Isosurfaces of  $\langle |\mathbf{L}| \rangle (D/U_H^2) = 0.7$ . (a) Isometric view of the measurement domain,  $\theta = 308^\circ$ ; (b)  $\theta = 20^\circ$ ; (c)  $\theta = 148^\circ$ ; (d)  $\theta = 276^\circ$ ; (e)  $\theta = 388^\circ$ . In panel (a), the black wire frame shows the total volume covered by the zoomed-in panels (b)–(e). The gray wire frame corresponds to the volume seen in panel (c). For panels (b)–(e), contour lines in the  $xz$  plane further illustrate the merging process between the two vortices. For visual clarity, the hub vortex has been masked from all panels.

be caused by reciprocal induction, but the difference in vortex strength results in significant velocity changes for only the green vortex.

A vortex-merging event occurs near  $x/D \approx 1.5$ , resulting in a single vortical structure downstream of this location. While such vortex merging has not been observed and/or reported by the wind-energy community, the interaction of two unequal, corotating vortices has been studied before (e.g., the numerical studies by Brandt and Nomura [45] and the combined numerical and experimental studies by Trieling *et al.* [46]). In this scenario the weaker vortex rapidly deforms, becoming encircled around the stronger vortex, which itself remains relatively unaffected. The same has also been observed and studied experimentally in shear layers (see for example [47]). This interaction was also experimentally studied for wake vortices originating from aircraft wings. By using two wings with different AoAs, Bertényi and Graham [48] were able to create two unequal, corotating vortices (meant to simulate the vortices shed from the slats/flaps on an aircraft in high lift/drag configuration) and saw the same phenomenon of the weaker vortex being rapidly deformed around the stronger vortex with little change to the properties of the stronger one. This was classified as “complete straining out” in the numerical studies by Dritschel and Waugh [49]. In the current study, evidence of this process can be observed, as the cyan vortical structure after merging is widened in the streamwise direction, but otherwise remains relatively unperturbed. This is seen in the contour lines in Figs. 3(d) and 3(e). Near-field vortex-merging corroborates the spectral analysis, where a peak at  $f_{BP}$  was absent downstream of this streamwise station in Figs. 2(b) and 2(c), and only a spectral peak at  $f_R$  was observed.

In conclusion, volumetric velocity measurements in the wake of a freely rotating wind turbine whose two rotor blades had different AoAs were presented. The downstream evolution of the tip vortices was analyzed through spectra and phase averaging the velocity fields. The tip vortices shed by the two rotor blades were observed to be different, both in size and strength, caused by the difference in AoA. The two vortices rapidly merge farther downstream, but do not follow the typical leapfrogging mechanism. As a consequence, the spectra showed a dominant peak at the rotational frequency and a smaller peak at the blade-pass frequency just downstream of the wind turbine. The smaller peak disappears after the vortex merging event. This demonstrates that observation of a single dominant spectral peak in a wind turbine wake at the rotational frequency, which has been observed in laboratory-scale experiments and in full-scale wind turbines, can result from the rotor

blades operating at different AoAs. While this was the cause here, any irregularities in the wind turbine's geometry arising from manufacturing tolerances or wear may lead to such a phenomenon. Given the importance of tip vortices in the wake recovery process, cataloging the various causes of such vortex dynamics is essential for wind energy production.

The data that support the findings herein are openly available from the NTNU Open Research repository [50].

- 
- [1] M. Toloui, L. P. Chamorro, and J. Hong, Detection of tip-vortex signatures behind a 2.5 MW wind turbine, *J. Wind Eng. Ind. Aerodyn.* **143**, 105 (2015).
  - [2] E. Barlas, S. Buckingham, and J. van Beeck, Roughness effects on wind-turbine wake dynamics in a boundary-layer wind tunnel, *Boundary Layer Meteorol.* **158**, 27 (2016).
  - [3] M. K. Vinnes, S. Gambuzza, B. Ganapathisubramani, and R. J. Hearst, The far wake of porous disks and a model wind turbine: Similarities and differences assessed by hot-wire anemometry, *J. Renewable Sustainable Energy* **14**, 023304 (2022).
  - [4] A reference to *Don Quixote* by Miguel de Cervantes. In modern usage, “tilting at windmills” refers to fighting imaginary enemies, according to Cambridge Dictionary.
  - [5] J. Whale, C. G. Anderson, R. Bareiss, and S. Wagner, An experimental and numerical study of the vortex structure in the wake of a wind turbine, *J. Wind Eng. Ind. Aerodyn.* **84**, 1 (2000).
  - [6] L. E. M. Lignarolo, D. Ragni, C. Krishnaswami, Q. Chen, C. J. Simão Ferreira, and G. J. W. van Bussel, Experimental analysis of the wake of a horizontal-axis wind-turbine model, *Renewable Energy* **70**, 31 (2014).
  - [7] M. Felli, R. Camussi, and F. D. Felice, Mechanisms of evolution of the propeller wake in the transition and far fields, *J. Fluid Mech.* **682**, 5 (2011).
  - [8] S. Ivanell, R. Mikkelsen, J. N. Sørensen, and D. Henningson, Stability analysis of the tip vortices of a wind turbine, *Wind Energy* **13**, 705 (2010).
  - [9] T. Sebastian and M. Lackner, Analysis of the induction and wake evolution of an offshore floating wind turbine, *Energies* **5**, 968 (2012).
  - [10] S. Sarmast, R. Dadfar, R. F. Mikkelsen, P. Schlatter, S. Ivanell, J. N. Sørensen, and D. S. Henningson, Mutual inductance instability of the tip vortices behind a wind turbine, *J. Fluid Mech.* **755**, 705 (2014).
  - [11] E. Kleusberg, R. F. Mikkelsen, P. Schlatter, S. Ivanell, and D. S. Henningson, High-order numerical simulations of wind turbine wakes, *J. Phys.: Conf. Ser.* **854**, 012025 (2017).
  - [12] V. G. Kleine, L. Franceschini, B. S. Carmo, A. Hanifi, and D. S. Henningson, The stability of wakes of floating wind turbines, *Phys. Fluids* **34**, 074106 (2022).
  - [13] L. Wang, W. Luo, and M. Li, Numerical investigation of a propeller operating under different inflow conditions, *Phys. Fluids* **34**, 105118 (2022).
  - [14] T. Maeda, Y. Kamada, J. Murata, S. Yonekura, T. Ito, A. Okawa, and T. Kogaki, Wind tunnel study on wind and turbulence intensity profiles in wind turbine wake, *J. Thermal Science* **20**, 127 (2011).
  - [15] W. Zhang, C. D. Markfort, and F. Porté-Agel, Near-wake flow structure downwind of a wind turbine in a turbulent boundary layer, *Exp. Fluids* **52**, 1219 (2012).
  - [16] L. J. Vermeer, J. N. Sørensen, and A. Crespo, Wind turbine wake aerodynamics, *Prog. Aero. Sciences* **39**, 467 (2003).
  - [17] I. V. Naumov, V. V. Rahmanov, V. L. Okulov, C. M. Velte, K. E. Meyer, and R. F. Mikkelsen, Flow diagnostics downstream of a tribladed rotor model, *Thermophys. Aeromech.* **19**, 171 (2012).
  - [18] Z. Yang, P. Sarkar, and H. Hu, Visualization of the tip vortices in a wind turbine wake, *J. Visualization* **15**, 39 (2012).
  - [19] D. van der Hoek, J. Frederik, M. Huang, F. Scarano, C. Simao Ferreira, and J.-W. van Wingerden, Experimental analysis of the effect of dynamic induction control on a wind turbine wake, *Wind Energy Science* **7**, 1305 (2022).

- [20] L. P. Chamorro, R. E. Arndt, and F. Sotiropoulos, Reynolds number dependence of turbulence statistics in the wake of wind turbines, [Wind Energy](#) **15**, 733 (2012).
- [21] S. Aubrun, S. Loyer, P. E. Hancock, and P. Hayden, Wind turbine wake properties: Comparison between a non-rotating simplified wind turbine model and a rotating model, [J. Wind Eng. Ind. Aerodyn.](#) **120**, 1 (2013).
- [22] P. E. Eriksen, Rotor Wake Turbulence: An Experimental Study of a Wind Turbine Wake, Ph.D. thesis, NTNU, 2016.
- [23] Y. Jin, H. Liu, R. Aggarwal, A. Singh, and L. P. Chamorro, Effects of freestream turbulence in a model wind turbine wake, [Energies](#) **9**, 830 (2016).
- [24] S. Rockel, J. Peinke, M. Hölling, and R. B. Cal, Dynamic wake development of a floating wind turbine in free pitch motion subjected to turbulent inflow generated with an active grid, [Renewable Energy](#) **112**, 1 (2017).
- [25] I. Neunaber, M. Hölling, R. J. Stevens, G. Schepers, and J. Peinke, Distinct turbulent regions in the wake of a wind turbine and their inflow-dependent locations: The creation of a wake map, [Energies](#) **13**, 5392 (2020).
- [26] P. E. Eriksen and P. Krogstad, Development of coherent motion in the wake of a model wind turbine, [Renewable Energy](#) **108**, 449 (2017).
- [27] Y. Jooss, L. Li, T. Bracchi, and R. J. Hearst, Spatial development of a turbulent boundary layer subjected to freestream turbulence, [J. Fluid Mech.](#) **911**, A4 (2021).
- [28] B. K. Smeltzer, O. Rømcke, R. J. Hearst, and S. Å. Ellingsen, Experimental study of the mutual interactions between waves and tailored turbulence, [J. Fluid Mech.](#) **962**, R1 (2023).
- [29] R. Ebenhoch, B. Muro, J.-Å. Dahlberg, P. B. Hägglund, and A. Segalini, A linearized numerical model of wind-farm flows, [Wind Energy](#) **20**, 859 (2017).
- [30] S. d. J. Helvig, M. K. Vinnes, A. Segalini, N. A. Worth, and R. J. Hearst, A comparison of lab-scale free rotating wind turbines and actuator disks, [J. Wind Eng. Ind. Aerodyn.](#) **209**, 104485 (2021).
- [31] A. Segalini and J.-Å. Dahlberg, Blockage effects in wind farms, [Wind Energy](#) **23**, 120 (2020).
- [32] A. Segalini and M. Chericoni, Boundary-layer evolution over long wind farms, [J. Fluid Mech.](#) **925**, A2 (2021).
- [33] M. K. Vinnes, N. A. Worth, A. Segalini, and R. J. Hearst, The flow in the induction and entrance regions of lab-scale wind farms, [Wind Energy](#) **26**, 1049 (2023).
- [34] C. Wang, F. Campagnolo, H. Canet, D. J. Barreiro, and C. L. Bottasso, How realistic are the wakes of scaled wind turbine models? [Wind Energy Science](#) **6**, 961 (2021).
- [35] T. Mücke, D. Kleinhans, and J. Peinke, Atmospheric turbulence and its influence on the alternating loads on wind turbines, [Wind Energy](#) **14**, 301 (2011).
- [36] D. Schanz, S. Gesemann, and A. Schröder, Shake-the-box: Lagrangian particle tracking at high particle image densities, [Exp. Fluids](#) **57**, 70 (2016).
- [37] B. Wieneke, Volume self-calibration for 3D particle image velocimetry, [Exp. Fluids](#) **45**, 549 (2008).
- [38] D. Schanz, S. Gesemann, A. Schröder, B. Wieneke, and M. Novara, Non-uniform optical transfer functions in particle imaging: calibration and application to tomographic reconstruction, [Meas. Sci. Technol.](#) **24**, 024009 (2013).
- [39] T. Janke and D. Michaelis, Uncertainty Quantification for PTV/ LPT data and Adaptive Track Filtering, in *14th International Symposium on Particle Image Velocimetry* (Paul V. Galvin Library/Illinois Institute of Technology, 2021), Vol. 1.
- [40] Y. J. Jeon, M. Müller, and D. Michaelis, Fine scale reconstruction (VIC#) by implementing additional constraints and coarse-grid approximation into VIC+, [Exp. Fluids](#) **63**, 70 (2022).
- [41] J. Z. Wu, H. Y. Ma, and M. D. Zhou, *Vorticity and Vortex Dynamics* (Springer, Berlin, Heidelberg, 2006).
- [42] T. Chen and T. Liu, Near-wall Lamb vector and its temporal–spatial evolution in the viscous sublayer of wall-bounded flows, [AIP Adv.](#) **12**, 035303 (2022).
- [43] S. Sunada, A. Sakaguchi, and K. Kawachi, Airfoil section characteristics at a low Reynolds number, [J. Fluids Eng.](#) **119**, 129 (1997).
- [44] J. Winslow, H. Otsuka, B. Govindarajan, and I. Chopra, Basic understanding of airfoil characteristics at low Reynolds numbers (104–105), [J. Aircr.](#) **55**, 1050 (2018).



- [45] L. K. Brandt and K. K. Nomura, Characterization of the interactions of two unequal co-rotating vortices, *J. Fluid Mech.* **646**, 233 (2010).
- [46] R. R. Trieling, O. U. Velasco Fuentes, and G. J. van Heijst, Interaction of two unequal corotating vortices, *Phys. Fluids* **17**, 087103 (2005).
- [47] H. S. Husain and F. Hussain, Experiments on subharmonic resonance in a shear layer, *J. Fluid Mech.* **304**, 343 (1995).
- [48] T. Bertényi and W. R. Graham, Experimental observations of the merger of co-rotating wake vortices, *J. Fluid Mech.* **586**, 397 (2007).
- [49] D. G. Dritschel and D. W. Waugh, Quantification of the inelastic interaction of unequal vortices in two-dimensional vortex dynamics, *Phys. Fluids* **4**, 1737 (1992).
- [50] <https://doi.org/10.18710/1NBWW5>.